Theory of simultaneous desalination and electricity generation via an electrodialysis cell driven by spontaneous redox reactions

I. Atlas [a, b], M.E. Suss [b, *]

[a] *Russell Berrie Nanotechnology Institute, Technion-Israel Institute of Technology, Haifa, 3200003, Israel*
[b] *Faculty of Mechanical Engineering, Technion-Israel Institute of Technology, Haifa, 3200003, Israel*

ARTICLE INFO

ABSTRACT

Electrodialysis (ED) is a well-established water desalination technology, applied mainly to brackish water desalination. In ED, desalination is driven by an applied electric field, which results in salt ion electromigration through alternating cation and anion exchange membranes. Recently, classical ED cells have been modified by driving them via spontaneous redox reactions occurring at the electrodes. Such a cell is distinct from classical ED as it does not require electricity, but rather requires solely chemical energy input in the form of redox active chemicals, and outputs both desalted water and electricity simultaneously. We here extend ED theory in order to capture a cell driven by spontaneous redox half-reactions occurring at electrode surfaces. In the cell considered, an AEM and CEM are separated by a channel with flowing feedwater. On the opposite side of the AEM is an anode and flowing anolyte, while a cathode and flowing catholyte are on the opposite side of the CEM. To capture cell behavior and performance at steady state, we solve a set of equations comprising the species' Nernst–Planck equation and electroneutrality, which are coupled to activation and concentration overpotential losses at planar electrodes. Our model captures the crossover of coion species through membranes as well as electric potential, counterion, and coion concentration variations within the membranes. We elucidate key predicted phenomena, including that the cell current is limited by reactant starvation at the cathode, and that current and certain ion fluxes scale as $x^{-1/3}$, where x is the coordinate in the direction of flow. Our model predicts that at steady state, the cell can achieve an order of magnitude reduction in the NaCl concentration of a 500 mM feed, while generating up to ~42 mW/cm^2 electrical power density. Further, we determined that the main limitation of the cell as designed is a relatively high coion crossover flux through the membranes.

© 2019 Elsevier Ltd. All rights reserved.

1. Introduction

The global increase in demand for potable water and energy, driven by increasing population and living standards, can be addressed via the development of innovative, scalable technologies to deliver low-cost clean energy and water. Further, there is an increasing interrelationship between these two commodities, known as the 'water-energy nexus' [1,2]. Energy production process, such as fuel extraction and processing, and electricity generation via thermoelectric, hydroelectric and other renewable technologies consume tremendous amount of water. Additionally, water desalination by reverse osmosis or electrodialysis [3], water

purification and softening, and wastewater remediation can require a substantial portion of the electricity supply. The most common desalination technique is sea water reverse osmosis (SWRO) delivering on the order of 10 million m^3 of treated water per day throughout the world. SWRO plants separate salt and water by pumping the feedwater through a semi-permeable membrane at a pressure above its osmotic pressure of ~25 bar [3,4]. To meet this high-pressure requirement, a city-scale SWRO requires a significant electricity input mainly to power high pressure pumps (~3–4 kWh/m^3 of desalted water).

One of the alternatives to SWRO for generating potable water is brackish water electrodialysis (ED) [5,6]. A typical ED cell requires an external power source to drive Faradaic reactions at electrodes, where these reactions enable continuous electromigration of salt ions from a diluate channel into an adjacent brine channel through ion exchange membranes [7–9]. When a voltage difference is

applied between the two electrodes, salt cations electromigrate towards the cathode. While an ideal anion-exchange membrane (AEM) completely blocks the salt cations, the cation-exchange membrane (CEM) allows cation transport from a diluate to an adjacent brine flow channel. Similarly, anions electromigrate towards the anode through an AEM but are blocked by a CEM. A typical ED stack consists of two electrodes separated by tens of alternating diluate and brine flow channels in parallel, with channels divided by either a cation or anion exchange membrane. While ED cells are highly scalable and can desalinate at low (sub-osmotic) pressures, they are generally not as energy efficient as RO when desalinating sea water [6]. Recently, ED has attracted renewed attention, with advances in understanding of overlimiting current mechanisms occurring at membrane surfaces underpinning novel cell architectures [10—14]. For example, in recently proposed shock ED, the basic ED cell is modified by including a weakly charged dielectric porous medium between similarly-charged membranes. The porous medium's surface charge enables transport via mechanisms of surface conduction or electroosmotic flow (depending on the pore size [14]). The salt transport dynamics during such a process give rise to an ion concentration shock wave emanating from a membrane surface, allowing for complete deionization of the feedwater not attainable via regular electrodialysis [15].

A common approach to the mathematical modelling of an ED cell is to invoke the Nernst—Planck equation [7—9,16—22] to describe ion fluxes due to advection, diffusion and electromigration. To solve for the local electric potential and concentration of all species, the complete set of equations includes the species' balance equations and either electroneutrality [7—9,17,23—27] or Poisson's equation. Poisson's equation, coupled with the Navier-Stokes and continuity equations, is invoked typically to study phenomena resulting from violations of electroneutrality near to the membrane surface, such as electroconvection vortices [14,28—33]. Water transport through the membranes can also be captured by considering water transport due to hydrostatic pressure gradients, osmosis, or electro-osmosis [8,34]. Membrane treatment can be simplified by considering membranes to be ideal, meaning perfectly selective and thus blocking coion flux completely [17,23,28,35,36]. The potential drop across an ideal membrane domain (when considered) is typically treated as an Ohmic potential drop [17,24,35]. Models which relax the ideal membrane assumption often include transport of both counterions and coions within the membranes [7—9,25,26,37,38]. In the latter models, the electroneutrality equation applied to the membrane includes the concentration of charged chemical groups, and further a hindered species diffusivity is used in the Nernst—Planck equations capturing ion transport in the membrane. To avoid resolving the nanoscale electric double layer (EDL) at the membrane/electrolyte interface, phase equilibrium is invoked so that the concentrations at each side of the interface can be related via a Boltzmann distribution.

Recently an ED cell driven by spontaneous redox reactions was proposed and characterized by Abu Khalla and Suss [39]. Unlike typical ED cells, the latter cell required only chemical energy as an input in the form of redox active chemicals, and outputted both desalted water and electricity simultaneously (see Fig. 1). As shown schematically in Fig. 1, this cell consists of an anion and cation exchange membrane separated by a channel fed with feedwater. On the opposite side of the AEM is an anode and anolyte, while a cathode and catholyte are on the opposite side of the CEM. During operation, the reductant and oxidant present in the anolyte and catholyte, respectively, react spontaneously at the electrode surfaces, thus generating a spontaneous ionic current through the cell which drives desalination in the feedwater channel. The AEM and CEM further act to electrostatically hinder the reductant and
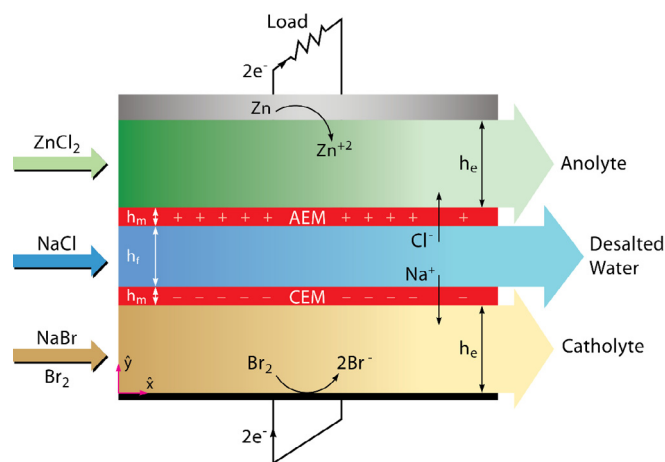

Fig. 1. Schematic of the ED cell modelled here, which is driven by spontaneous electrochemical reactions occurring at electrodes. An AEM and CEM are separated by a desalination channel fed with feedwater. On the opposite side of the AEM is an anode and anolyte, while a cathode and catholyte are on the opposite side of the CEM. During operation, the reductant and oxidant present in the anolyte and catholyte, respectively, react spontaneously at the anode and cathode, generating electric current and driving ion removal from the desalination channel.
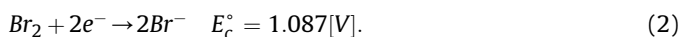
oxidant, respectively, from entering the desalination channel. We here extend ED theory to include cells driven by spontaneous electrode reactions, and study the desalination and electricity generation of such a cell. The model is of a complete cell including a planar anode, anolyte, planar cathode, catholyte, AEM, and CEM, and accounts for coion crossover through the finite-thickness membranes, as well as overpotential losses at electrodes. For ~30 mA/cm^2 extracted current density, predictions demonstrate up to an order of magnitude reduction in NaCl concentration from inlet to outlet with a 500 mM NaCl feed, simultaneously to electricity generation with up to ~42 mW/cm^2 delivered power density. We elucidate key factors affecting cell performance, such as those limiting desalination performance and electricity generation. For example, one limitation observed with the design studied here was high coion crossover rates through membranes, which inhibited the desalination extent and limited local membrane current efficiency to below ~0.7 at the model conditions investigated. Thus, our model can serve as a valuable tool to gain insight into the performance of ED cells driven by spontaneous reactions, and in the future to predict data and guide the optimization of experimental cells.

2. Mathematical model

To model and study the cell shown in Fig. 1, we couple elements of established electrodialysis models [7] together with elements of fuel cell or flow battery models [40—43]. This coupling allows us to capture the transport of species through electrolyte solutions and membranes, where ionic current through the cell is driven by spontaneous redox reactions occurring at electrode surfaces. We investigate the removal of sodium chloride (NaCl) from feedwater, when the cell is driven by zinc oxidation at the anode,

$$Zn \rightarrow Zn^{+2} + 2e^- \quad E_a^\circ = -0.762[V] , \qquad (1)$$
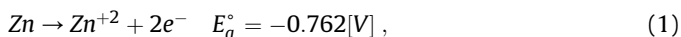
and bromine reduction at the cathode,

$$Br_2 + 2e^- \rightarrow 2Br^- \quad E_c^\circ = 1.087[V]. \qquad (2)$$

Here $E^\circ{}_a$ and $E^\circ{}_c$ are the standard reduction potentials for the oxidation and reduction half-reactions, respectively. The overall cell

reaction is,

$$Zn + Br_2 \rightarrow Zn^{+2} + 2Br^-. \tag{3}$$

Zinc-bromine chemistry is investigated here as it is known to be a high-performance chemistry, with fast electrochemical reactions at electrodes (anodic exchange current density ~1 mA/cm² and cathodic exchange current density ~10^{-3} mA/cm²), and compatible with highly conductive electrolytes (>100 mS/cm at room temperature) [44]. However, in the future other chemistries optimized for performance, low cost, or safety can be modelled with the same approach we develop here. In our model, the catholyte is comprised of an aqueous solution containing $NaBr$ and Br_2, while the anolyte is aqueous $ZnCl_2$. While the cell is fed with reactants, here Zn metal and Br_2, it will desalinate continuously in a manner similar to a typical ED cell, albeit without requiring any electricity input.

2.1. Governing equations

In our model, there are 6 unknown variables, including the concentrations of zinc ions, $c_{Zn^{+2}}$, bromide, c_{Br^-}, bromine, c_{Br_2}, sodium ions, c_{Na^+}, chloride, c_{Cl^-} and the electrostatic potential ϕ. For simplicity, we assume steady state, dilute solutions, and neglect bromine/bromide complexation in the catholyte [41]. We can then write a mass balance equation for each species, i, present in the system, as

$$\nabla \cdot \overline{N}_i = 0. \tag{4}$$

Here $\overline{N}_i$ is the molar flux of species i, which we can describe via the Nernst−Planck (NP) equation,

$$\overline{N}_i = \overline{u} c_i - D_{eff,i}(\nabla c_i + z_i c_i \nabla \widehat{\phi}). \tag{5}$$

Here c_i is the concentration of species i, z_i is its valence, and $D_{eff,i}$ is the effective diffusivity of species i, which deviates from the molecular diffusivity in the membrane phase. The parameter $\widehat{\phi}$ is the dimensionless electric potential, where potential is scaled by the thermal voltage $V_T = RT/F$, and F is Faraday's constant, R is the ideal gas constant, and T is the absolute temperature. We define the effective diffusivity of species i as

$$D_{eff,i}(y) = D_i - D_i \cdot (1 - d)(\Pi_{CEM} + \Pi_{AEM}). \tag{6}$$

where D_i is the molecular diffusivity of species i at infinite dilution, and d is a diffusivity reduction factor in the membrane [7,45,46]. Further, Π_{AEM} and Π_{CEM} are smoothed boxcar functions defined as unity within the AEM and CEM bulk, and zero in the bulk of the flow channels (see Section 2.1.1). We consider 2D rectangular geometry as shown in Fig. 1 and 1D laminar Poiseuille flow in the x-direction in each flow channel [40,41], given by

$$\overline{u} \cdot \widehat{x} = 6U_k \left(\frac{y_k}{h_k} - \frac{y_k^2}{h_k^2} \right) \tag{7}$$

where U_k, h_k and y_k are the channel area average velocity, height and relative vertical coordinate of channel k, respectively (see Table 1). We complete the set of equations with the electroneutrality condition,

$$\sum_i z_i c_i + X_m (\Pi_{AEM} - \Pi_{CEM}) = 0 \tag{8}$$

where X_m is the concentration of charged groups per volume of electrolyte in the membrane [7–9,45–47]. We further replace the Br^- balance equation (Eq. (4) applied to Br^-), with a charge balance

equation given by $\sum z_i \nabla \cdot \overline{N}_i = 0$. By defining ionic current density, $\overline{J} = F \sum z_i \overline{N}_i$, we can write the charge balance equation as $\nabla \cdot \overline{J} = 0$. Including a charge balance equation enables our use of boundary conditions for the model which involve ionic current (see Table 2 and Eq. (14)).

2.1.1. Membrane/electrolyte interface

One approach towards modeling the membrane/electrolyte interface is to resolve explicitly the concentration and potential distribution in the nanoscale EDL at such interfaces, for example by invoking the Poisson equation [36,48–50]. An alternate strategy is to instead define separate electroneutrality and Nernst−Planck equations for the electrolyte and membrane sub-domains and connect them via a Boltzmann distribution, $c_{m,i} = c_{e,i} \exp(-z_i \Delta \widehat{\phi}_D)$, and the continuity of ion flux [7–9,45,46]. Here $c_{m,i}$ is the concentration of species i at the membrane side of the interface, $c_{e,i}$ is the concentration at the electrolyte side, and $\Delta \widehat{\phi}_D$ is the non-dimensional Donnan potential drop across the interface. Such a model introduces apparent jump discontinuities in ion concentration and potential across the membrane/electrolyte boundary. The Boltzmann distribution is obtained when assuming that the membrane and solution remain in phase equilibrium with zero net species flux across the interface.

In our model, we do not explicitly resolve the EDL (do not invoke the Poisson equation), and furthermore we do not invoke the Boltzmann distribution. Instead, to allow for a relatively simple numerical implementation, we consider a single domain including all membranes and channels, and in it invoke mass balance equations given by Eq. (4), the ionic charge balance equation in Section 2.1, and the electroneutrality condition given by Eq. (8). We describe the shift in effective diffusivity and fixed charge along the membrane/electrolyte interface with continuous smoothed boxcar functions defined as a superposition of smoothed step functions, $\Pi_{CEM} \approx 0.5 \cdot [erfc(-(y_f + h_m)/\tau) - erfc(-y_f/\tau)]$ and $\Pi_{AEM} \approx 0.5 \cdot [erfc(-(y_a + h_m)/\tau) - erfc(-y_a/\tau)]$. Here h_e, h_f and h_m is the thickness of the anolyte or catholyte flow channel, feedwater channel, and each membrane, respectively (see Fig. 1). Further, y_f and y_a are the relative vertical coordinates of the feed and anolyte channels, respectively (see Table 1). The parameter τ is the length of transition (smoothing) zone between the bulk and membrane phases, which are used in order to prevent infinite gradients in the numerical implementation of the model ($\tau = \beta h_m$, where $\beta = 0.01$, see Table 1).

2.2. Boundary conditions

A typical ED system consists of repeating unit cells which contain a concentrate channel, a CEM, a diluate channel, and an AEM. A simplification often used in ED models assumes binary and symmetric salts and symmetric membranes with equal charge density magnitude [7,8,17,23]. These assumptions allow for assuming a symmetry midplane in each channel in which a zero flux boundary condition is applied. Thus, several previous ED models [7–9,23] consider domains comprised of one half of a concentrate channel, one membrane (either a CEM or AEM) and one half of a diluate channel. However, in our cell, the feedwater (diluate) channel is bounded by anolyte and catholyte channels (see Fig. 1). Thus, for our cell, symmetry boundary conditions in the middle of channels would not be appropriate, and the model domain must include the entire cell.

We start with the electrode boundary conditions. Using generalized notation, a Faradaic half-cell reaction can be expressed as [51].

Table 1
Model parameters used in all simulation results given in this Section.

Parameter	Symbol	Value
Temperature	T	$298 K$
Bromide diffusivity	D_{Br^-}	$2.08 \cdot 10^{-5} \ cm^2/s$ [40,41]
Bromine diffusivity	D_{Br_2}	$1.15 \cdot 10^{-5} \ cm^2/s$ [40,41]
Zinc diffusivity	$D_{Zn^{+2}}$	$0.754 \cdot 10^{-5} \ cm^2/s$ [53]
Membrane diffusivity reduction factor	d	0.1
Channel length	L	$6.7 \ cm$
Membrane charge concentration	X_m	$2 \ M$
Anolyte and catholyte channel thickness	h_e	$2 \ mm$
Feed channel thickness	h_f	$1 \ mm$
Membrane thickness	h_m	$127 \ \mu m$
Transition zone length	τ	$1.27 \ \mu m$
Anolyte velocity	U_a	$1 \ mm/s$
Catholyte velocity	U_c	$1 \ mm/s$
Feedwater velocity	U_f	$0.278 \ mm/s$
Anolyte relative vertical coordinate	y_a	$y - h_e - h_f - 2h_m$
Catholyte relative vertical coordinate	y_c	y
Feed channel relative vertical coordinate	y_f	$y - h_e - h_m$
$ZnCl_2$ inlet concentration	$c_{ZnCl_2,in}$	$1 \ M$
$NaBr$ inlet concentration	$c_{NaBr,in}$	$1 \ M$
Br_2 inlet concentration	$c_{Br_2,in}$	$0.5 \ M$
$NaCl$ inlet concentration	$c_{NaCl,in}$	$0.5 \ M$
Anode exchange current density	J_a	$1 \ A/cm^2$ [53,54]
Cathode exchange current density	J_c	$3.1 \cdot 10^{-3} \ A/cm^2$ [53,54]
Standard cathode potential	$E°_c$	$1.087 \ V$ [40,41]
Standard anode potential	$E°_a$	$-0.762 \ V$ [55]

*cell thickness is $h = 2h_e + 2h_m + h_f$

Table 2
Summary of boundary conditions invoked at the planar electrodes.

	Anode $y = h$	Cathode $y = 0$	
$\hat{n} \cdot \vec{J} =$	j_a	j_c	Current continuity
$\hat{n} \cdot \vec{N}_{Zn^{+2}} =$	$j_a/2F$	0	Faraday's law
$\hat{n} \cdot \vec{N}_{Br_2} =$	0	$j_c/2F$	Faraday's law
$\hat{n} \cdot \vec{N}_{Na^+} =$	0	0	Non-reactive species
$\hat{n} \cdot \vec{N}_{Cl^-} =$	0	0	Non-reactive species

*$\hat{n}$ is the surface normal vector (pointing into the cell).

Table 3
Summary of inlet boundary conditions at x = 0.

	Catholyte	Middle channel	Anolyte
$c_{Zn^{+2}} =$	0	0	$c_{ZnCl_2,in}$
$c_{Br_2} =$	$c_{Br_2,in}$	0	0
$c_{Br^-} =$	$c_{NaBr,in}$	0	0
$c_{Na^+} =$	$c_{NaBr,in}$	$c_{NaCl,in}$	0
$c_{Cl^-} =$	0	$c_{NaCl,in}$	$2c_{ZnCl_2,in}$

$$\sum_i s_i R_i^{z_i} \rightarrow \sum_j s_j O_j^{z_j} + ne^-, \tag{9}$$

where s and z represent the stoichiometric coefficients and valence, respectively, of reduced state species R_i or oxidized state species O_j participating in an n electron transfer reaction. We describe the current generated by the electrochemical reaction given in Eq. (9) at a planar electrodes using the symmetric Butler-Volmer equation (symmetric transfer coefficient, $\alpha = 0.5$ [40,52]),

$$j = 2J_o \sqrt{\hat{c}_O \hat{c}_R} \sinh\left(\frac{n\eta}{2}\right) \tag{10}$$

where $\hat{c}_O \equiv \prod_i \hat{c}_i^{s_i}$ and $\hat{c}_R \equiv \prod_j \hat{c}_j^{s_j}$ are the dimensionless surface

activities of the oxidized state species and the reduced state species respectively, and J_o is the exchange current density. We define a dimensionless electrode overpotential as $\eta \equiv \varphi^s - \varphi^e - \theta_{a/c}$ [42,43,53], where φ^s is the dimensionless electrode potential and φ^e is the dimensionless electrolyte potential at the electrode surface, and all potentials are normalized by the thermal voltage, V_T. The relative dimensionless local open-circuit potential, $\theta_{a/c}$, of the anode or cathode is given by Ref. [53]:

$$\theta_{a/c} = \frac{F}{RT}\left(E°_{a/c} - E°_a\right) - \frac{1}{n}\ln\left(\frac{\hat{c}_R}{\hat{c}_O}\right) \tag{11}$$

The difference $E°_{a/c} - E°_a$ represents the standard reduction potential of the anode or cathode relative to the standard anode reduction potential $E°_a$. For the anode, we consider unity zinc activity at the anode, and thus the relative anode open-circuit potential is $\theta_a = 0.5\ln(\hat{c}_{Zn^{+2}})$. We assume that the anode is grounded, so that $\varphi^s = 0$ for the anode, and the anodic overpotential is $\eta_a = -\hat{\phi}(y = h) - 0.5\ln(\hat{c}_{Zn^{+2}})$, where $h = 2h_e + 2h_m + h_f$ is the cell thickness (see Fig. 1). Using Eq. (10), we develop the following expression for current at the anode,

$$j_a = -2J_a\sqrt{\hat{c}_{Zn^{+2}}}\sinh\left[\hat{\phi}(y = h) + \frac{1}{2}\ln(\hat{c}_{Zn^{+2}})\right]. \tag{12}$$

Here J_a is the exchange current density of the anode half-reaction. At the cathode, the relative local open-circuit potential is given by $\theta_c = \hat{E}_{OCV} + 0.5\ln[\hat{c}_{Br_2}/(\hat{c}_{Br^-})^2]$, where $\hat{E}_{OCV} = (E°_c - E°_a)/V_T$. The cathode voltage is given by $\varphi^s_c = V_{cell}$, and thus the cathodic overpotential is $\eta_c = \hat{V}_{cell} - \hat{\phi}(y = 0) - \hat{E}_{OCV} - 0.5\ln[\hat{c}_{Br_2}/(\hat{c}_{Br^-})^2]$. Finally, the cathodic current can be written as

$$j_c = -2J_c\hat{c}_{Br^-}\sqrt{\hat{c}_{Br_2}}\sinh\left[\hat{\phi}(y = 0) - V_{cell} + \hat{E}_{OCV} + \frac{1}{2}\ln\left(\frac{\hat{c}_{Br_2}}{\hat{c}_{Br^-}^2}\right)\right]. \tag{13}$$

where J_c is the exchange current density of the cathode half-

reaction. For the boundary conditions at the anode and cathode, we invoke current continuity at the electrode surface, and calculate Zn^{+2} and Br_2 fluxes via Faraday's law (see Table 2) [40,41]. The fluxes of electrochemically inert species at these boundaries, Na^+ and Cl^-, are set to zero.

At the inlet of the cell, we impose fixed concentration boundary conditions for all species in all three channels, (see Fig. 1 and Table 3). We further impose zero normal ionic current at both the inlet and the outlet,

$$\bar{J}(x=0) \cdot \hat{n} = \bar{J}(x=L) \cdot \hat{n} = 0. \tag{14}$$

At the outlet, we set the species flux equal to the advective flux in all channels,

$$\overline{N}_i \big|_{x=L} \cdot \hat{n} = -(\overline{u} \cdot \hat{x}) \cdot c_i \tag{15}$$

The molar flux at the upstream and downstream edges of the membranes is set to zero,

$$\overline{N}_i \big|_{x=0} \cdot \hat{n} = \overline{N}_i \big|_{x=L} \cdot \hat{n} = 0 \tag{16}$$

3. Results and discussion

To solve equations (4)-(16), we performed 2D simulations in the finite element framework of COMSOL Multiphysics with direct solver MUMPS and a rectangular mesh. In Table 1, we list the parameters used in the simulations. Fig. 2 shows the predicted non-dimensional Na^+ and Cl^- concentration profiles in the feedwater channel, for a cell voltage well below the open circuit voltage, which was $V_{cell} = 0.9\ V$. Both Na^+ and Cl^- concentration profiles show significant reduction in concentration between the inlet and outlet of the feedwater channel, which demonstrates the potential effectiveness of our cell towards water desalination. For example, in Fig. 2a, normalized Na^+ concentration drops from unity at the inlet ($x/L = 0$) to as low as ~0.2 at the outlet ($x/L = 1$) of the feedwater channel. Thus, as in previous ED models [7,17,25], the selective transport of ions through the membranes results in significant depletion of salt ions in the feed channel. However, in those models, desalination was driven by an externally applied voltage but for our cell, no external power is applied, but rather ionic current arises due to spontaneous electrochemical reactions occurring at the electrodes. Differences in local concentration between Na^+ and Cl^- ions are observed in Fig. 2, as Na^+ concentration at the outlet is a minimum near to the AEM ($y/h \sim 0.55$), and at a maximum near to the CEM ($y/h \sim 0.45$), but Cl^- is highest near to the CEM, and lowest near to the AEM. Such an imbalance between Na^+ and Cl^- concentrations would not be expected for ideal membranes, however in our model the membranes are not ideal as they permit some coion crossover.

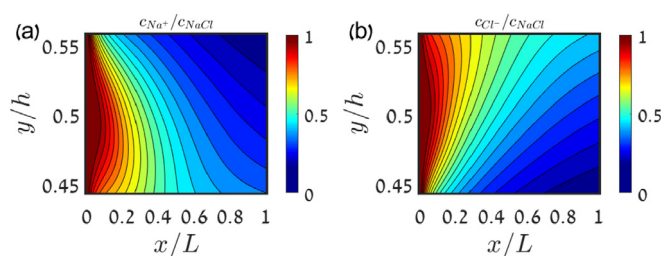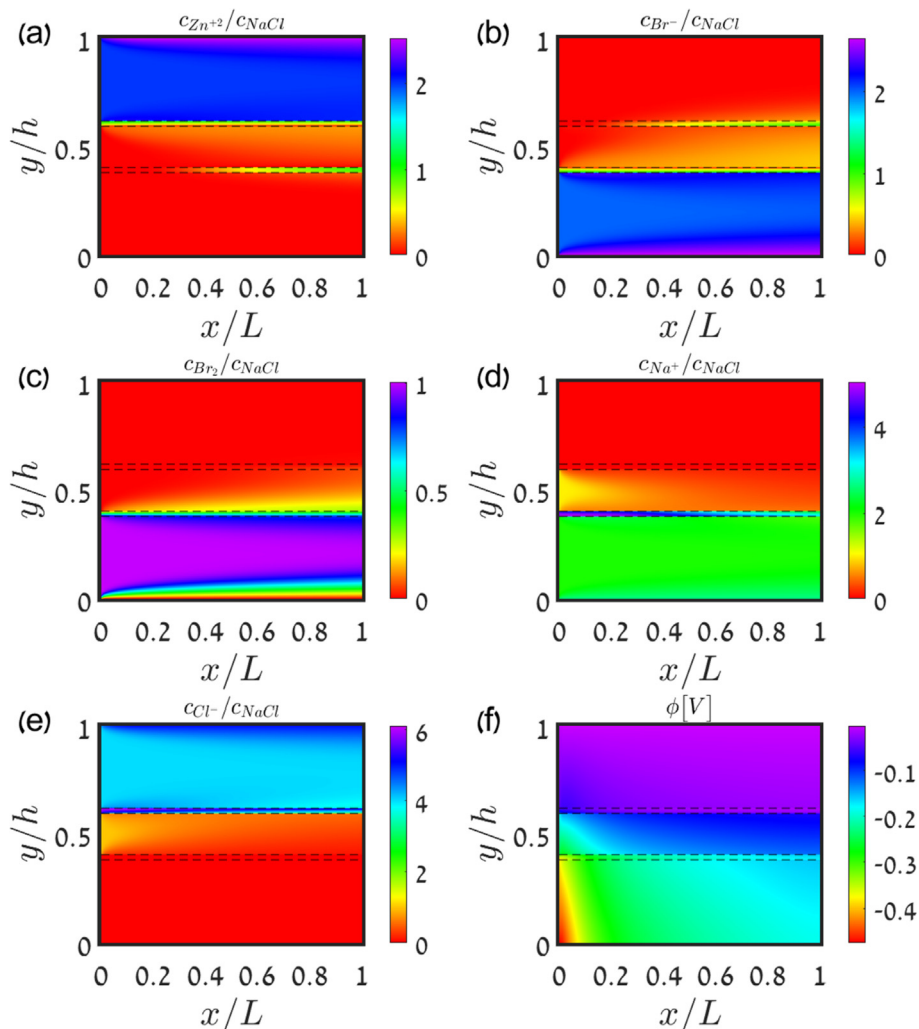In Fig. 3, we plot model predictions of species concentrations

Fig. 2. Model predictions of salt ion concentration in the feed channel, normalized by the inlet NaCl concentration with (a) showing Na^+ concentration and (b) Cl^- concentration.

and potential throughout the cell, for $V_{cell} = 0.9V$. In Fig. 3a, we show the prediction for Zn^{2+} concentration, where the inlet non-dimensional concentration in the anolyte, from $y/h \sim 0.6$ to $y/h = 1$, is two, while in the feed channel ($y/h \sim 0.4$ to $y/h \sim 0.6$) and catholyte ($y/h = 0$ to $y/h \sim 0.4$) the inlet concentration is zero. We can observe Zn^{2+} crossover through the AEM ($y/h \sim 0.6$), as a Zn^{2+} mass transport boundary layer in the feed channel adjacent to the AEM. At the feed channel outlet, the non-dimensional Zn^{+2} concentration rises as high as ~0.5, indicating significant crossover. Further, we see an accumulation of Zn^{+2} in the CEM ($y/h \sim 0.4$), reaching a concentration of up to ~1 within this membrane. In Fig. 3b and c, we observe catholyte Br^- and Br_2 crossover boundary layers in the feed channel and along the CEM, respectively. The non-dimensional Br^- concentration in the feed channel rises as high as ~0.5 at the outlet, while the Br_2 concentration in the feed channel rises to ~0.25 at the outlet. Further, we see accumulation of Br^- within the AEM, where it reaches a concentration of ~1. Results also show that Br^- transports from the catholyte all the way into the anolyte via the AEM (Fig. 3b). Thus, our model predicts significant crossover of various species, which suggests future cells should be designed to reduce species concentration gradients across adjacent flow channels. We note that our model likely overestimates the Br_2 and Br^- crossover flux which would be attained in an analogous experimental cell, as Br_2 and Br^- complex together the form Br_3^-, where the latter is typically the dominant oxidant species [41]. Such complexation chemistry, and its effect on species crossover and cell performance, is outside the scope of this work.

As expected from the overall cell reaction (Eq. (3)), during operation an enrichment concentration boundary layer develops near the anode ($y/h = 1$ in Fig. 3a) due to the production of Zn^{+2}, and at the cathode ($y/h = 0$ in Fig. 3b) due to the production of Br^-. Further, a Br_2 depletion boundary layer develops at the cathode due to consumption of Br_2 (Fig. 3c). Braff et al. [40] and Ronen et al. [41] described Br_2 depletion boundary layers along planar cathodes in models of membraneless hydrogen-bromine flow batteries. In the cell of Braff et al., transport of Br_2 across the cathode boundary layer determined the limiting (maximum) current achievable by the cell during discharge [40]. At our cell voltage of 0.9 V, we can see that the Br_2 concentration approaches zero at the cathode (Fig. 3c). This indicates that at this voltage, our system is at its limiting current, and that our cell's current is likewise limited by Br_2 transport to the cathode. This is a counterintuitive result, as naively one could expect that the cell's limiting current would be attributable to salt depletion at membrane interfaces in the feed channel, as in ED cells. However, the diffusive crossover of Zn^{+2} from the anolyte and Br^- from catholyte into the feed channel, together with coion electromigration through the membrane, replenish the diluate feed channel with ions. While our cell is limited by Br_2 reduction, note that in typical ED cells, limiting current is only achieved when approaching zero ion concentration at the diluate channel/membrane interface [7,56].

While Fig. 2 shows concentration profiles for the Na^+ and Cl^- in the feed channel, Fig. 3d and e show the concentration profile for Na^+ and Cl^-, respectively, across the entire cell. In both figures we see the depletion of salt from the middle channel and accumulation of Na^+ in the CEM ($y/h \sim 0.4$) and Cl^- within the AEM ($y/h \sim 0.6$). In Fig. 3f, we plot the model solution for potential, and observe that the highest potentials are attained along the anode ($y/h = 1$), and a gradual potential drop occurs within flow channels along the cell's y-direction. Further, we observe sharp potential drops at the membrane\electrolyte interface ($y/h \sim 0.4$ and $y/h \sim 0.6$ receptively), which appear qualitatively similar to Donnan potential drops [25,47]. However, in our model these potential drops are not due to the imposition of phase equilibrium across the membrane/electrolyte interface, but rather arise from flux and current continuity

Fig. 3. Model predictions of species concentrations and electric potential throughout the cell, for (a) Zn^{+2}, (b) Br^-, (c) Br_2, (d) Na^+, (e) Cl^- and (f) ϕ. All concentrations are normalized by the inlet NaCl concentration of the feedwater channel. The dashed horizontal lines represent the membrane boundaries.

across this interface. Further, in Fig. 3f, we see that the highest electric field is attained at the inlet ($x/L=0$) and that the field decreases fairly sharply with x near to the inlet.

Fig. 4a shows the magnitude of the predicted cathodic current density $|j_c|$, vs. x/L for the case of $V_{cell} = 0.9$ V (solid blue line). The highest local current density of ~55 mA/cm² is attained at the inlet, $x/L=0$, and local current density decreases along the length of the cell, to ~20 mA/cm² at the outlet, giving a cathode-area averaged density of ~30 mA/cm². The decay in current with x can be attributed largely to the growth of the Br_2 depletion boundary layer at the cathode (Fig. 3c), which results in increasingly sluggish Br_2 transport to the cathode with increasing x/L. In Fig. 4a, we also show $|j_c|$ scaled by $(x/L)^{-1/3}$ (dashed green line), and we can see that this scaled current is roughly constant when plotted vs. x/L. A scaling of cell current with $(x/L)^{-1/3}$ has been obtained from analytical solutions to the concentration field in a thin Br_2 boundary layer at the limiting current, upon implementing a Leveque approximation for the velocity through the layer [40]. Thus, our results in Fig. 4a inset show that the same scaling largely applies in our cell, evidence of the important role of the Br_2 boundary layer along the cathode on cell performance.

To quantify species crossover, in Fig. 4b and c we plot predicted species flux at the membrane midplane for the case of $V_{cell} = 0.9$ V.

We can see that the AEM (Fig. 4b) permits significant Cl^- flux (yellow line), with maximal flux of N_{Cl^-}~4 mmol/m²s attained near the channel inlet ($x/L=0$). The latter flux approximately scales as $x^{-1/3}$, indicating that this is the primary current carrying ion through the AEM. We further observe Br^- transport (green line) from the feed channel to the anolyte channel through the AEM, which occurs because of Br^- crossover into the feed channel from the catholyte (see Fig. 3b). In Fig. 4b, we can see that $N_{Br^-} = 0$ at the inlet as there is no Br^- at the location of the AEM, but rises to 1 mmol/m²s at the outlet. Also seen in Fig. 4b is that Zn^{+2} coions permeate through the AEM to the feed channel (blue line). The highest crossover flux of $N_{Zn^{+2}}$~ −1 mmol/m²s is attained at the inlet and decreases along the length of the cell. In Fig. 4c we show predicted fluxes through the CEM and observe that a maximum removal of N_{Na^+}~-4 mmol/m²s is attained near the channel inlet and Na^+ flux approximately scales as $x^{-1/3}$, indicating that Na^+ is the primary current carrying ion through the CEM. Slight transport of Zn^{+2} (blue line) is also observed through the CEM from the feed channel to the catholyte. Neutrally charged Br_2 (red line) and Br^- ions (green line) permeate from the catholyte through the CEM to the feed channel. The highest Br^- crossover flux of N_{Br^-}~2 mmol/m²s is attained at the inlet, and decreases along the length of the cell, while N_{Br_2} is nearly constant with x.
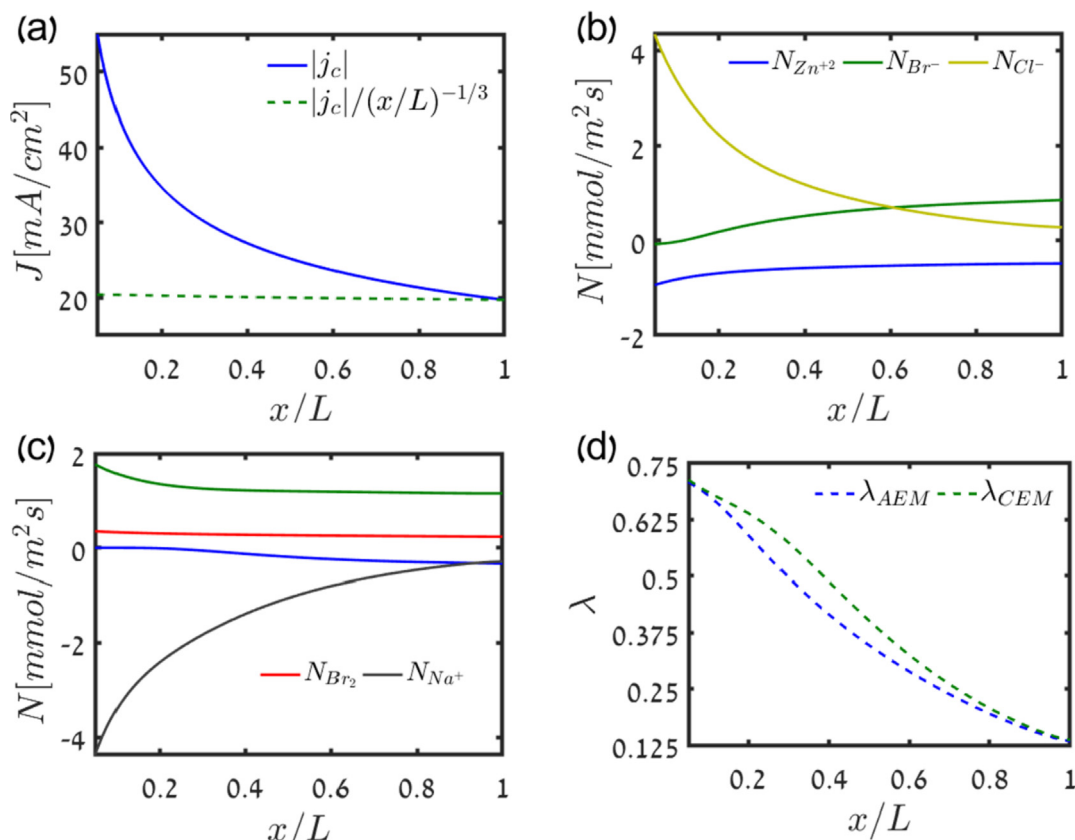
Fig. 4. Model predictions for: (a) Cathodic current density (solid blue line) and scaled cathodic current density (dashed green line) vs. x/L. (b) AEM midplane ion fluxes. Positive flux describes ion remval from the feed channel (c) CEM midplane ion fluxes. Negative flux describes ion remval from the feed channel (d) Membrane local current efficiency.

In Fig. 4d we show the calculated local current efficiency at the membrane midplane, defined as $\lambda_{AEM/CEM} = \left| N_{Cl^-/Na^+} / \sum_i z_i N_i \right|$, vs. x/L. Ideal AEMs and CEMs would allow only Cl^- and Na^+ transport, respectively, yielding $\lambda_{AEM/CEM} = 1$. For non-ideal membranes, the flux of other species through the membrane reduces the current efficiency. For our cell, the highest predicted local current efficiency of $\lambda_{CEM} \sim 0.7$ is obtained at the inlet, $x/L=0$, and we can observe that both λ_{CEM} and λ_{AEM} decrease with x/L to a minimum value of $\lambda_{AEM} \sim 0.1$ at the outlet. The decrease of $\lambda_{AEM/CEM}$ with x/L indicates an increasing fraction of total current carried by ions not in the feedwater (Zn^{2+} and Br^-) with x/L. In Fig. 4d, we can also see that the predicted current efficiency of the AEM is generally lower than that attributed to the CEM for the same location, x/L. This is likely due to transport of Br^- through the AEM, up to $N_{Br^-} \sim 1$ mol/m²s (see Fig. 4b), as significant Br^- reaches the AEM from the catholyte due to its relatively high diffusivity (see Table 1). We can compare our current efficiency to that predicted for regular ED cells driven by electricity. For example, Tedesco et al. [7] predicted a current efficiency of *>0.5* at all locations along their AEM and CEM for the same membrane charge used in this work ($X_m = 2$ M). The latter comparison emphasizes that a main limitation in the performance of our proposed ED cell is high membrane crossover. Future designs should endeavor to reduce ion concentration gradients across membranes, in an effort to achieve current efficiencies rivaling that of traditional ED.

Fig. 5 shows predictions of electric potential at the cell midplane, $x/L = 0.5$, when the cell is operated at the limiting current, $V_{cell} = 0.9$ V, and when operated near to equilibrium, $V_{cell} = 1.8$ V (the open-circuit voltage is ~1.808 V), as function of y/h. Near to

equilibrium, the cell current density is near zero, and the potential is approximately uniform across each channel and membrane in the cell. However, sharp variations in potential are observed at the membrane/electrolyte interface, which can be described as Donnan potentials. These potential drops are not symmetric across a given membrane, leading to a non-zero membrane potential, which is due to concentration differences of ions between the flow channels sandwiching each membrane at equilibrium [38,47,57—59]. For example, at 1.8 V, the AEM membrane potential is ~8 mV while the CEM membrane potential is ~24 mV. By contrast, at the lower cell voltage associate with the limiting current, we observe that the potential drop across channels and within membranes is significant and shows a roughly linear profile. At the membrane/electrolyte interfaces, we again see the sharp variations in potential, which arises from a conservation of mass and current across these interfaces (we here did not impose phase equilibrium across these interfaces). The membrane potential is significantly higher when far from equilibrium, with 55 mV for the AEM and 328 mV for the CEM.

We next define an ion removal factor, κ, as the ratio between the outlet mass flow rate of species in the feed channel to that of the inlet,

$$\kappa = \frac{\int_0^{h_f} [\overline{u}(y_t) \cdot \hat{x}] \cdot \sum_i c_i(x = L, y_t) \cdot dy}{2U_f c_{NaCl,in} h_f}. \tag{17}$$

Fig. 6 shows the predicted ion removal factor κ (solid green curve), calculated using Eq. (17) and summed over all ions in the cell, and desalination factor κ_{NaCl} (green dashed curve), calculated
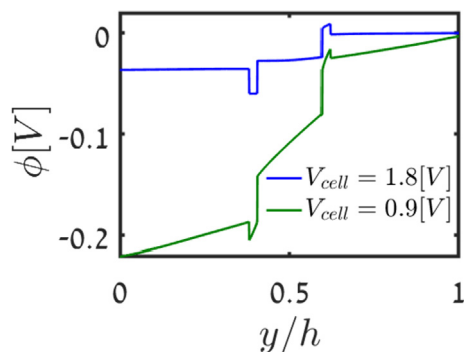
Fig. 5. Predicted potential profile in the cell at $x/L = 0.5$, showing profiles both across membrane/electrolyte interfaces, and within membranes and channels themselves. Results are shown for a cell voltage of 1.8 V, which captures the cell behavior close to equilibrium (close to open circuit voltage), and for a cell voltage of 0.9 V for behavior far from equilibrium.

using Eq. (17) summed over only Na^+ and Cl^-, both as function of cell current density. For current densities less than 4 mA/cm^2, the feed channel receives net NaCl ($\kappa_{NaCl} > 1$) due to diffusion-driven crossover of Na^+ across the AEM and Cl^- across the CEM. For current densities between 4 mA/cm^2 and 12 mA/cm^2, NaCl is net removed from the feed channel ($\kappa_{NaCl} < 1$), but replaced with Zn^{+2}, Br^- and Br_2 due crossover of these species across the membranes ($\kappa > 1$). For current densities greater than 12 mA/cm^2, our cell removes net ions from the feedwater, so that both κ_{NaCl} and κ are smaller than unity. That ion removal factor is greater than unity even for moderate current density demonstrates again that coion crossover is a key limiting issue and reducing crossover should be addressed in a future work.

To quantify the cell electricity generation occurring simultaneously to the desalination, we use a polarization curve (Fig. 6 blue curve). The maximal output voltage seen on the polarization curve, 1.808 V, is the open-circuit voltage (OCV) attained at zero current. Irreversible frictional losses decrease the output voltage from the OCV as current is increased (as we depart further from equilibrium) [60]. The roughly linear profile of the polarization curve for current densities below about 25 mA/cm^2 indicates that Ohmic potential drops across channels and membranes dominate losses at these currents. Concentration overpotential losses, due largely to Br_2

depletion at the cathode, results in non-linear profile seen at high current densities near-to the limiting current of 30 mA/cm^2. The delivered electrical power density of the cell is given by the multiplication of cell voltage by extracted current density, $P = V_{cell} \cdot j$. This power density increases with current density until reaching limiting current, with a maximum delivered power density of ~42 mW/cm^2 attained at ~29 mA/cm^2. In addition to the electrical power delivered, we can calculate the power input to the cell at a given current density, a chemical energy input, by multiplying the cell's OCV by the current density $P_{chem} = V_{OCV} \cdot j$ [39]. This quantity also represents the electrical power density which would be attained had the chemical-to-electrical energy conversion been lossless. For example, at the condition of maximum power density ($j = 29$ mA/cm^2), P_{chem} ~52.2 mW/cm^2. We define the net power consumption of the cell, as chemical power input minus electrical power recovered, $P_{net} = P_{chem} - P$. Thus, the net power density consumption of our cell at the condition of maximum electrical power density is P_{net} ~10.2 mW/cm^2. Finally, we can calculate the specific chemical energy consumption of the cell by dividing the net power required by the cell by the volumetric flow rate in the feed channel $EC = P_{net}/(u_f h_f)$ [7]. At the maximum power density, where κ_{NaCl} ~0.3 (Fig. 6), we obtain EC ~6.8 kWh/m^3.
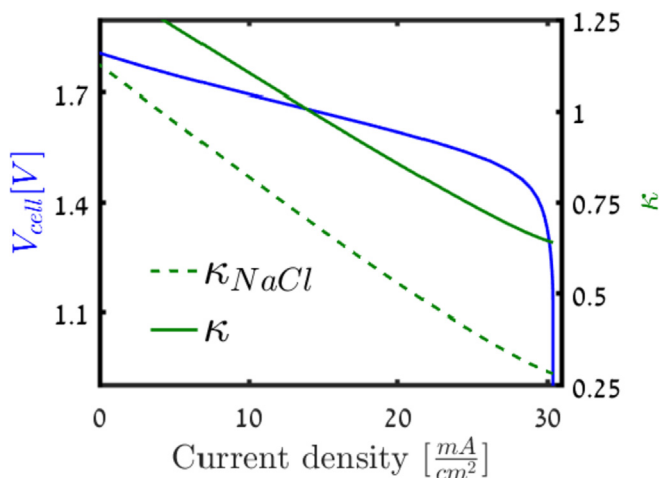
4. Conclusion

In this work, we extended ED theory to cells driven by spontaneous redox reactions, demonstrating simultaneous desalination and electricity generation due to a chemical-to-electrical energy conversion process. We present results showing key features in our ED cell's operation, and quantified performance for a cell based on high performance Zn—Br$_2$ chemistry. We demonstrate that the main limitation of the cell as designed here is expected to be a relatively high coion crossover into the feedwater channel. Thus, this model can guide us to next-generation designs targeting reduced coion crossover, in which desalination performance and energy efficiency can be greatly improved. In the future, the model framework developed here can be applied to different redox chemistries, cell geometries, and for membranes with varying properties, and should be validated with a dedicated set of experimental results.

Fig. 6. Predicted cell voltage, V_{cell} (blue line, left y-axis), ion removal factor κ (green line, right y-axis) and desalination factor κ_{NaCl} (green dashed line, right y-axis) as function of cell current density.

References

[1] S. Pritchard, The water-energy nexus, Int. Water Power Dam Constr. 65 (2013) 42—45.
[2] M.W. Shahzad, M. Burhan, L. Ang, K.C. Ng, Energy-water-environment nexus underpinning future desalination sustainability, Desalination 413 (2017) 52—64.
[3] N. Ghaffour, T.M. Missimer, G.L. Amy, Technical review and evaluation of the economics of water desalination: current and future challenges for better water supply sustainability, Desalination 309 (2013) 197—207.
[4] M. Elimelech, W.A. Phillip, The future of seawater desalination: energy, technology, and the environment, Science 333 (2011) 712—717.
[5] A. Campione, L. Gurreri, M. Ciofalo, G. Micale, A. Tamburini, A. Cipollina, Electrodialysis : a critical assessment an overview of recent developments on process fundamentals , models and applications, Desalination 434 (2018) 121—160.
[6] H. Strathmann, Electrodialysis, a mature technology with a multitude of new applications, Desalination 264 (2010) 268—288.
[7] M. Tedesco, H.V.M. Hamelers, P.M. Biesheuvel, Nernst-Planck transport theory for (reverse) electrodialysis: I. Effect of co-ion transport through the

membranes, J. Membr. Sci. 510 (2016) 370—381.

[8] M. Tedesco, H.V.M. Hamelers, P.M. Biesheuvel, Nernst-Planck transport theory for (reverse) electrodialysis: II. Effect of water transport through ion-exchange membranes, J. Membr. Sci. 531 (2017) 172—182.

[9] K. Tado, F. Sakai, Y. Sano, A. Nakayama, An analysis on ion transport process in electrodialysis desalination, Desalination. 378 (2016) 60—66.

[10] D. Deng, E.V. Dydek, J.H. Han, S. Schlumpberger, A. Mani, B. Zaltzman, M.Z. Bazant, Overlimiting current and shock electrodialysis in porous media, Langmuir 29 (2013) 16167—16177.

[11] D. Deng, W. Aouad, W.A. Braff, S. Schlumpberger, M.E. Suss, M.Z. Bazant, Water purification by shock electrodialysis: deionization, filtration, separa-tion, and disinfection, Desalination 357 (2015) 77—83.

[12] S. Schlumpberger, N.B. Lu, M.E. Suss, M.Z. Bazant, Scalable and continuous water deionization by shock electrodialysis, Environ. Sci. Technol. Lett. 2 (2015) 367—372.

[13] L. Alvarado, A. Chen, Electrodeionization: principles, strategies and applica-tions, Electrochim. Acta 132 (2014) 583—597.

[14] F. Roghmans, E. Evdochenko, F. Stockmeier, S. Schneider, A. Smailji, R. Tiwari, A. Mikosch, E. Karatay, A. Kühne, A. Walther, A. Mani, M. Wessling, 2D Patterned Ion-Exchange Membranes Induce Electroconvection, Adv. Mater. Interfaces. 6 (2019) 1—11.

[15] D. Desai, E.S. Beh, S. Sahu, V. Vedharathinam, Q. Van Overmeere, C.F. De Lannoy, A.P. Jose, A.R. Völkel, J.B. Rivest, Electrochemical desalination of seawater and hypersaline brines with coupled electricity storage, ACS Energy Lett 3 (2018) 375—379.

[16] T. Teorell, Transport processes and electrical phenomena in ionic membranes, Prog. Biophys. Biophys. Chem. 3 (1953) 305—369.

[17] A.A. Sonin, R.F. Probstein, A hydrodynamic theory of desalination by elec-trodialysis, Desalination 5 (1968) 293—329.

[18] A.G. Guzmán-Garcia, P.N. Pintauro, M.W. Verbrugge, R.F. Hill, Development of a space-charge transport model for ion-exchange membranes, AIChE J. 36 (1990) 1061—1074.

[19] M. Higa, A. Tanioka, K. Miyasaka, An experimental study of ion permeation in multicomponent ion systems as a function of membrane charge density, J. Membr. Sci. 64 (1991) 255—262.

[20] V. Fíla, K. Bouzek, A mathematical model of multiple ion transport across an ion-selective membrane under current load conditions, J. Appl. Electrochem. 33 (2003) 675—684.

[21] V.M. Volgin, A.D. Davydov, Ionic transport through ion-exchange and bipolar membranes, J. Membr. Sci. 259 (2005) 110—121.

[22] M. Fidaleo, M. Moresi, Optimal strategy to model the electrodialytic recovery of a strong electrolyte, J. Membr. Sci. 260 (2005) 90—111.

[23] R.F. Probstein, Physicochemical Hydrodynamics : an Introduction, second ed., Wiley-Interscience, Hoboken, N.J, 2003.

[24] J.G.D. Tadimeti, V. Kurian, A. Chandra, S. Chattopadhyay, Corrugated mem-brane surfaces for effective ion transport in electrodialysis, J. Membr. Sci. 499 (2016) 418—428.

[25] L. Gurreri, G. Battaglia, A. Tamburini, A. Cipollina, G. Micale, M. Ciofalo, Multi-physical modelling of reverse electrodialysis, Desalination 423 (2017) 52—64.

[26] A.A. Moya, Numerical simulation of ionic transport processes through bilayer ion-exchange membranes in reverse electrodialysis stacks, J. Membr. Sci. 524 (2017) 400—408.

[27] V. Geraldes, M.D. Afonso, Limiting current density in the electrodialysis of multi-ionic solutions, J. Membr. Sci. 360 (2010) 499—508.

[28] V.S. Pham, Z. Li, K.M. Lim, J.K. White, J. Han, Direct numerical simulation of electroconvective instability and hysteretic current-voltage response of a permselective membrane, Phys. Rev. E - Stat. Nonlinear Soft Matter Phys. 86 (2012) 1—11.

[29] A.V. Kovalenko, N.D. Pismenskaya, P. Sistat, J. Han, V.V. Nikonenko, G. Pourcelly, M.K. Urtenov, Desalination at overlimiting currents: state-of-the-art and perspectives, Desalination 342 (2014) 85—106.

[30] N.A. Mishchuk, Electro-osmosis of the second kind near the heterogeneous ion-exchange membrane, Colloids Surfaces A Physicochem. Eng. Asp. 140 (1998) 75—89.

[31] I. Rubinstein, B. Zaltzman, Electro-osmotically induced convection at a permselective membrane, Phys. Rev. E 62 (2000) 2238—2251.

[32] I. Rubinstein, Electroconvection at an electrically inhomogeneous permse-lective interface, Phys. Fluids A. 3 (1991) 2301—2309.

[33] Y. Green, G. Yossifon, Dynamical trapping of colloids at the stagnation points of electro-osmotic vortices of the second kind, Phys. Rev. E - Stat. Nonlinear Soft Matter Phys. 87 (2013) 1—9.

[34] C. Jiang, Q. Wang, Y. Li, Y. Wang, T. Xu, Water electro-transport with hydrated

[35] Z. Zourmand, F. Faridirad, N. Kasiri, T. Mohammadi, Mass transfer modeling of desalination through an electrodialysis cell, Desalination 359 (2015) 41—51.

[36] A.A. Moya, Electrochemical impedance of ion-exchange membranes with interfacial charge transfer resistances, J. Phys. Chem. C 120 (2016) 6543—6552.

[37] A.A. Moya, A numerical comparison of optimal load and internal resistances in ion-exchange membrane systems under reverse electrodialysis conditions, Desalination 392 (2016) 25—33.

[38] A.A. Moya, A Nernst-Planck analysis on the contributions of the ionic trans-port in permeable ion-exchange membranes to the open circuit voltage and the membrane resistance in reverse electrodialysis stacks, Electrochim. Acta 238 (2017) 134—141.

[39] S. Abu Khalla, M.E. Suss, Desalination via chemical energy: An electrodialysis cell driven by spontaneous electrode reactions, Desalination. 467 (2019) 257—262.

[40] W.A. Braff, C.R. Buie, M.Z. Bazant, Boundary layer analysis of membraneless electrochemical cells, J. Electrochem. Soc. 160 (2013) A2056—A2063.

[41] R. Ronen, I. Atlas, M.E. Suss, Theory of flow batteries with fast homogeneous reactions, J. Electrochem. Soc. 165 (2018) 3820—3827.

[42] A.Z. Weber, J. Newman, Modeling Transport in Polymer-Electrolyte Fuel Cells, 2004.

[43] A.Z. Weber, R.L. Borup, R.M. Darling, P.K. Das, T.J. Dursch, W. Gu, D. Harvey, A. Kusoglu, S. Litster, M.M. Mench, R. Mukundan, J.P. Owejan, J.G. Pharoah, M. Secanell, I.V. Zenyuk, A critical review of modeling transport phenomena in polymer-electrolyte fuel cells, J. Electrochem. Soc. 161 (2014) F1254—F1299.

[44] A.A. Chilenskas, E.C. Gay, R.K. Steunenberg, H.S. Lim, A.M. Lackner, R.C. Knechtli, Zinc-Bromine Secondary Battery (1978) 1154—1157.

[45] J.E. Dykstra, K.J. Keesman, P.M. Biesheuvel, A. van der Wal, Theory of pH changes in water desalination by capacitive deionization, Water Res. 119 (2017) 178—186.

[46] J.M. Paz-Garcia, J.E. Dykstra, P.M. Biesheuvel, H.V.M. Hamelers, Energy from CO2 using capacitive electrodes - a model for energy extraction cycles, J. Colloid Interface Sci. 442 (2015) 103—109.

[47] J.M. Paz-Garcia, O. Schaetzle, P.M. Biesheuvel, H.V.M. Hamelers, Energy from CO2 using capacitive electrodes - theoretical outline and calculation of open circuit voltage, J. Colloid Interface Sci. 418 (2014) 200—207.

[48] B. Zaltzman, I. Rubinstein, Electro-osmotic slip and electroconvective insta-bility, J. Fluid Mech. 579 (2007) 173—226.

[49] M.A.K. Urtenov, E.V. Kirillova, N.M. Seidova, V.V. Nikonenko, Decoupling of the Nernst-Planck and Poisson equations. Application to a membrane system at overlimiting currents, J. Phys. Chem. B 111 (2007) 14208—14222.

[50] S.A. Mareev, D.Y. Butylskii, N.D. Pismenskaya, V.V. Nikonenko, Chro-nopotentiometry of ion-exchange membranes in the overlimiting current range. Transition time for a finite-length diffusion layer: modeling and experiment, J. Membr. Sci. 500 (2016) 171—179.

[51] J. Newman, K.E. Thomas-Alyea, Electrochemical Systems, third ed., Wiley-Interscience, Hoboken, N.J, 2004.

[52] D.P. Scamman, G.W. Reade, E.P.L. Roberts, Numerical modelling of a bromide-polysulphide redox flow battery. Part 1: modelling approach and validation for a pilot-scale system, J. Power Sources 189 (2009) 1220—1230.

[53] M.J. Mader, R.E. White, A mathematical model of a Zn/Br2 cell on charge, J. Electrochem. Soc. 133 (1986) 1297.

[54] G.D. Simpson, R.E. White, R.E. White, An algebraic model for a zinc/bromine flow cell, J. Electrochem. Soc. 136 (1989) 9—16.

[55] P. Vanýsek, Electrochemical series, in: J.R. Rumble (Ed.), CRC Handb. Chem. Phys., 99th ed., CRC Press/Taylor & Francis, Boca Raton, FL, 2018.

[56] J.C. De Valença, R.M. Wagterveld, R.G.H. Lammertink, P.A. Tsai, Dynamics of microvortices induced by ion concentration polarization, Phys. Rev. E - Stat. Nonlinear Soft Matter Phys. 92 (2015) 1—5.

[57] K.W. Knehr, E.C. Kumbur, Open circuit voltage of vanadium redox flow bat-teries: discrepancy between models and experiments, Electrochem. Commun. 13 (2011) 342—345.

[58] K.W. Knehr, E. Agar, C.R. Dennison, A.R. Kalidindi, E.C. Kumbur, A transient vanadium flow battery model incorporating vanadium crossover and water transport through the membrane, J. Electrochem. Soc. 159 (2012) A1446—A1459.

[59] A.H. Galama, J.W. Post, H.V.M. Hamelers, V. V Nikonenko, P.M. Biesheuvel, On the origin of the membrane potential arising across densely charged ion ex-change membranes: how well does the teorell-meyer-sievers theory work? J. Membr. Sci. Res. 2 (2016) 128—140.

[60] R.P. O'Hayre, Fuel Cell Fundamentals, Wiley, Hoboken, NJ, 2016.